Supporting Information

Spider-web inspired multi-resolution graphene tactile sensor

Lu Liu,†[a, b] Yu Huang,†[b] Fengyu Li,*[b] Ying Ma,*[a] Wenbo Li,[b] Meng Su,[b] Xin Qian,[b] Wanjie Ren,[b] Kanglai Tang[c] and Yanlin Song*[b]

Abstract: Multi-dimensional accurate response and signal smooth transmission critically challenge the advancement of multi-resolution recognition and complex environment analysis. Inspired by the structure-activity relationship of discrepant microstructures of spiral and radial threads in spider web, we designed and printed graphene porous and dense-packing microstructure to integrate multi-resolution graphene tactile sensor. The three-dimensional (3D) graphene porous structure performs multi-dimensional deformation responses. The laminar graphene dense-packing structure contributes excellent conductivity with flexible stability. The spider-web inspired printed pattern inherits orientational and locational kinesis tracking. Multi-structure construction with homo-graphene material can integrate discrepant electronic properties with remarkable flexibility, which will attract the enormous pursuits of electronic skin, wearable devices and human-machine interaction.

DOI: 10.1002/anie.2016XXXXX

Table of Contents

Experimental section 2
Preparation of GO ink 2
Fabrication of the sensor 2
Characterization 2
Data Analysis 2
Control circuit of the mechanical palm 2
Additional experimental data 3

[a] *School of Materials Science and Engineering, Shenyang Jianzhu University, Shenyang 110168, P. R. China*

[b] *Key Laboratory of Green Printing, Institute of Chemistry, Chinese Academy of Sciences (ICCAS); Beijing Engineering Research Center of Nanomaterials for Green Printing Technology; Beijing National Laboratory for Molecular Sciences (BNLMS); Beijing 100190, P. R. China. E-mail: forrest@iccas.ac.cn; may171@iccas.ac.cn; ylsong@iccas.ac.cn*

[c] *Sports Medicine Center, Southwest Hospital, Third Military Medical University, Chongqing 400038, China*

† These authors contributed equally.

Electronic Supplementary Information (ESI) available: [details of any supplementary information available should be included here]. See DOI: 10.1039/x0xx00000x

Fig. S1. SEM image of GO 3
Fig. S2. AFM image of GO 3
Fig. S3. Raman spectra of the GO and rGO 4
Fig. S4. XRDpatterns of the GO and rGO 4
Fig. S5. Force-time curve recorded before and after graphene aerogel left graphene ribbon 6

Fig. S6. The schematic diagram of structural change for the graphene aerogel under mechanical deformation 6
Fig. S7. Raman spectra and XRD patterns of graphene ribbon before cycling and after 1000 cycles 5
Fig. S8. Raman spectra and XRD patterns of graphene aerogel before cycling and after 1000 cycles 5
Fig. S9. The cross image of tactile sensor with PDMS packaging 5
Fig.S10. The real-timemonitoring of resistance changes 7
Fig. S11. Electronic discriminant analysis of random positions based on the graphene tactile sensor 7
Fig.S12. PCA score plots of the first three principal components of P1-P6 8
Fig.S13. PCA score plots of the first three principal components of P7-P12 9
Fig.S14. PCA score plots of the first three principal components of P13-P18 10
Table S1 Linear discriminant analysis (LDA) of P1-P12 11
Table S2 Linear discriminant analysis (LDA) of P13-P18 11
Fig. S15. Control circuit of the mechanical palm 12
References 12

Experimental Section

Preparation of GO ink

3 g expandable graphite, 2.5 g $K_2S_2O_8$ and 2.5 g P_2O_5 were successively added into 40 mL concentrated H_2SO_4 (98%) with stirring. The mixture was heated to 80 °C and kept for 5 hours. The mixture was cooled down naturally to the room temperature and diluted with ice water. After filtering with 2 L deionized water, the preoxidized graphite was obtained by drying at room temperature for 2 days. Then the pre-oxidized graphite was added into 120 mL concentrated H_2SO_4 using an ice bath, and 9 g $KMnO_4$ was added slowly with stirring. The mixture was stirred at 35 °C for 2 hours, then diluted with ice water after cooling down to the room temperature. 15 mL H_2O_2 (30%) was added dropwise until the mixture color become bright yellow. The supernatant was poured out after resting 12 hours. The remaining precipitate was washed with deionized water, 10% hydrochloric acid, deionized water in turn and centrifuged. The remaining precipitate was put in dialysis bag until pH=7. The as-prepared GO dispersion was stirred in a 60 °C water bath to prepare ink with concentration of 15 mg/mL.

Fabrication of the sensor

The GO ink was loaded in a syringe (3 cm^3 barrel) with a micronozzle (200 μm inner diameter) and printed by using a multiaxis dispensing system (2400, EFD). The radiations were printed according to previously setting pattern and dried in an ambient atmosphere for 3 hours. Then the spirals were printed on the dry patterns, frozen in liquid nitrogen and put in a -25 °C refrigerator for 12 hours. The printed pattern was vacuum freezing-dried at -60 °C for 3 hours. Next, the printed pattern was immersed by HI (15%) aqueous solution, heated to 95 °C and kept for 3 hours. After cooling to room temperature, the pattern was washed three times with deionized water and frozen in liquid nitrogen and put in a -25 °C refrigerator for 12 hours. The pattern was vacuum-dried at -60 °C for 3 hours. The PDMS mixture of base and cross-linker (the weight ratio of base to cross linker was 10:1) was stirred until the mixture was even and degassed in vacuum for 30 min to remove bubbles at room temperature. Then PDMS mixture was poured over the printed pattern except the electrodes. Finally, the pattern was dried in an ambient atmosphere for 30 min, then solidified at 80 °C for 3 hours.

Characterization

The samples were characterized using field emission scanning electron microscopy (FE-SEM, Hitachi S4800), atomic force microscope (AFM, Bruker Multimode 8), Raman spectroscope (LabRAM HR Evolution) with a laser excitation wavelength of 532 nm, X-ray diffraction (XRD, Empyrean) using monochromatic Cu Kα1 radiation (λ = 1.5406 Å) at 40 kV. The resistances of samples were characterized by four-probe method (Keithley 4200 Semiconductor Characterization System) and HIOKI RM3545 resistance meter. The strains were applied by using a home-made stretching equipment. Each data point was tested at least 5 samples, and average values were used for the plots. The adhesive force between graphene aerogel and ribbon was measured using a force gauge (Mark 10, M5-5, Series 5). Multianalysis was conduct by the multichannel recorder (HIOKI, LR8400).

Data Analysis

Principal component analysis (PCA), hierarchical clustering analysis (HCA) and linear discriminant analysis (LDA) were performed using Minitab v16.1.1.0. They were conducted to accurately classify and correctly cluster through the responses from multi-structure graphene tactile sensor stimulated different positions. Five characteristic values were read out at the peak or nadir of the monitoring resistance curves by the electronic data logger. Each position was tested for 9 times and had 55 variables to describe the responses on the sensor.

Control circuit of the mechanical palm

As shown in the circuit diagram (Figure S15), the graphene pattern and a 1K resistor are connected in series. When the graphene aerogel is subjected to certain stress, the resistance changes, resulting the change of voltage. Arduino mega 2560 is the core circuit board. It has 54 digital input/output pins, 4 universal asynchronous receiver/transmitter (UARTs, hardware serial ports), a 16 MHz crystal oscillator, a USB connection, a power jack, an ICSP header, and a reset button. The 5 analog voltages are added to the analog input port A0-A4 of the mega 2560, and 5 digital quantities can be obtained. The procedure in the mega 2560 judges 5 digital quantities and detects which graphene

aerogel is pressed. At the same time, mega 2560 sends corresponding control instructions to the steering engine controller through the serial port. Steering engine controller based on control instructions outputs specific command to the steering engine. The steering engine receives the pulse width modulation (PWM) wave, rotates and drives the movement of the mechanical finger.

Additional experimental data

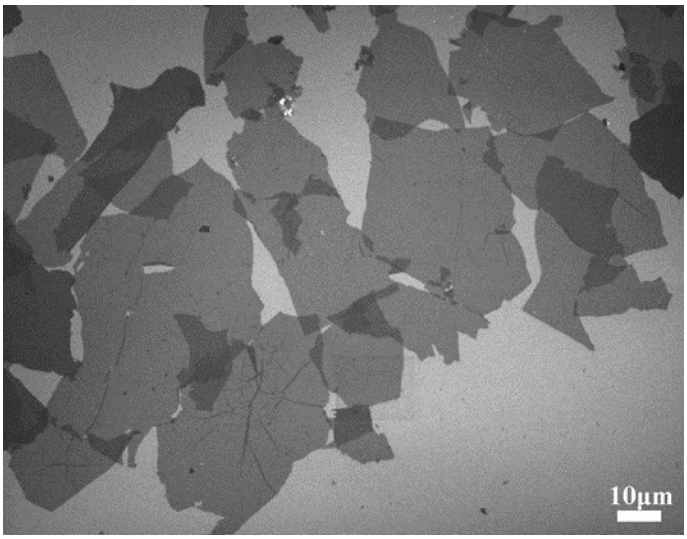

Fig. S1 SEM image of GO. The lateral sizes of GO sheets distribute from 16.7 μm to 83.3 μm.

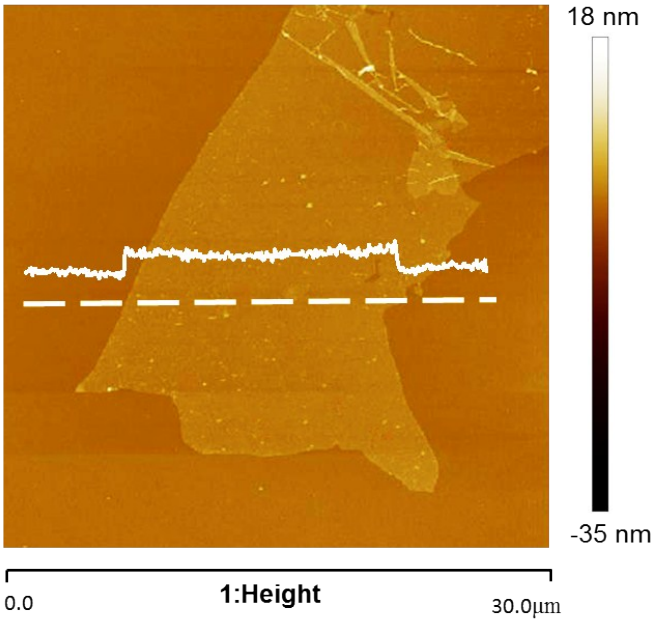

Fig. S2 AFM image of GO. The typical thickness is characterized as 0.95 nm.

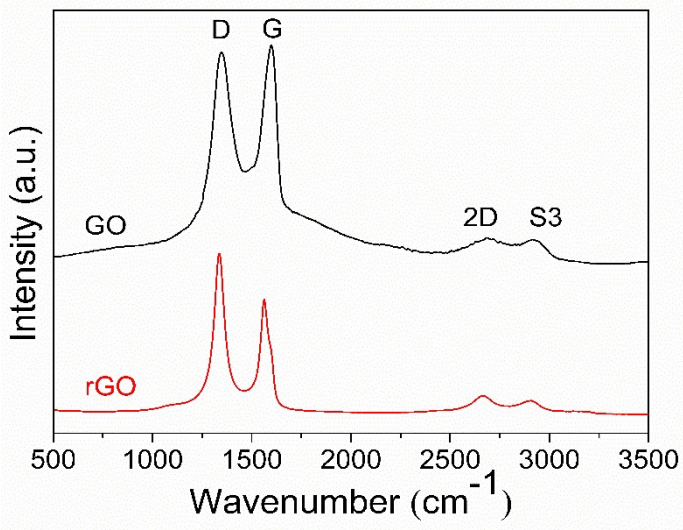

Fig. S3 Raman spectra of the GO and rGO. The increase of I_D/I_G ratio reveals the partial restoration of C sp^2 in the rGO. The increase of the I_{2D}/I_{S3} ratio further indicates restoration of the conjugation structure after reduction.

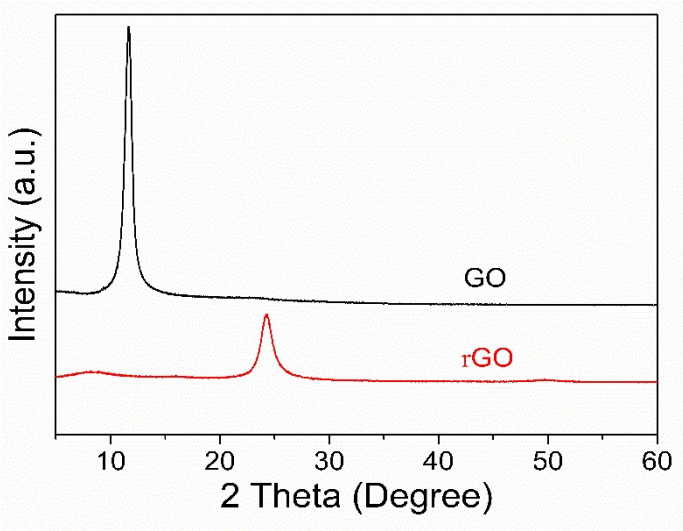

Fig S4 XRD patterns of the GO and rGO. The d spacing of GO and rGO are 7.59Å and 3.66Å, respectively. The decreasing interlamellar spacing is due to partial removal of the oxygen-containing groups after reduction.

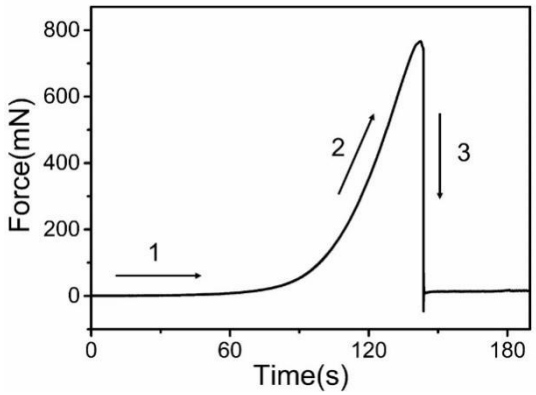

Fig. S5 Force-time curve recorded before and after graphene aerogel left graphene ribbon. Graphene aerogel contacted with graphene ribbon while maintaining the force at zero (process 1). Graphene aerogel was moved up at the rate of 0.26 mm/min. When graphene aerogel left graphene ribbon, the force increased gradually and reached its maximum at the end of process 2. Finally, the force decreased immediately when the graphene ribbon broke away from graphene aerogel in process 3. The maximum adhesive force between graphene aerogel and ribbon is about 766.5 mN, when the contact area was 4 cm×0.55 cm.

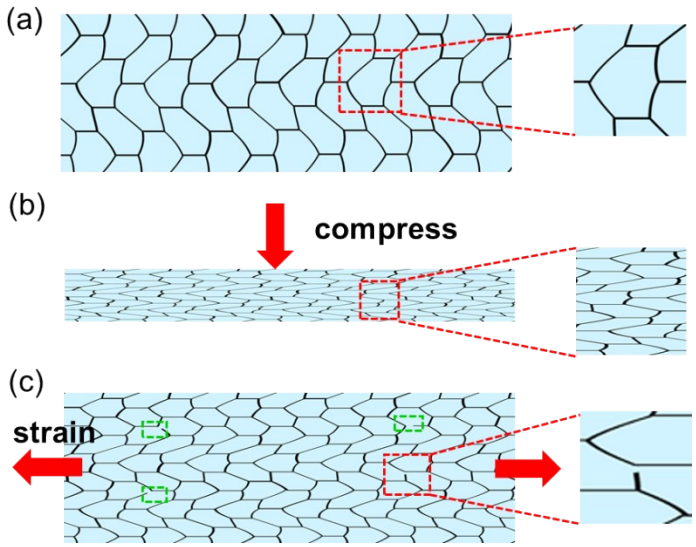

Fig. S6 The schematic diagram of structural change for the graphene aerogel under mechanical deformation. (a) Orignal structural state of the graphene aerogel. (b) Structural change of the graphene aerogel under compression. (c) Structural change of the graphene aerogel under strain. When the graphene aerogel is compressed, the graphene sheets become compact, which results in the increase of connected area between graphene sheets and the decrease of the resistance. When the graphene aerogel is strained, the graphene sheets become separate, resulting in the decrease of connected area between graphene sheets and the increase of the resistance. When the strain is removed, the graphene sheets reconnected gradually because of the reversion of the PDMS elastomer. The structural change of graphene aerogel under other mechanical tests is a combination of the above two types of deformation.

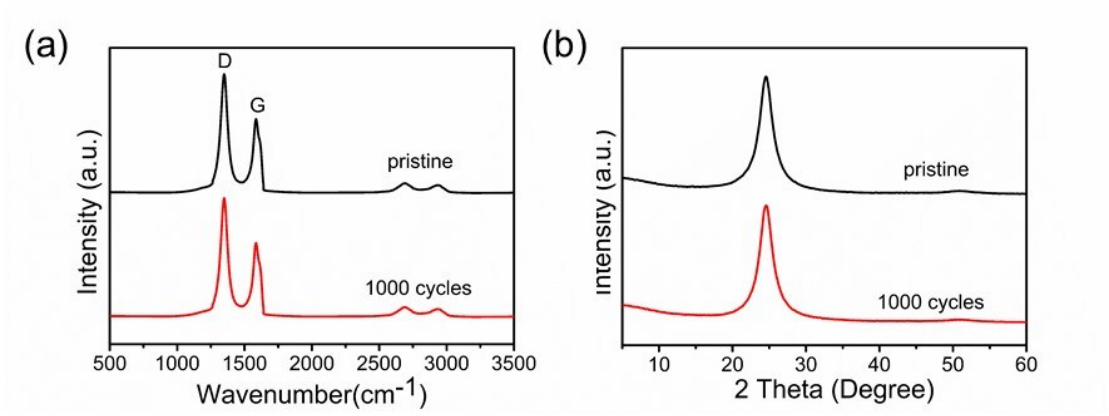

Fig S7 (a) Raman spectra and (b) XRD patterns of graphene ribbon before cycling and after 1000 cycles. The samples were subjected to 1000 cycles under 90° blending without PDMS. No obvious variations in either the G and D peak positions or the I_D/I_G ratio were observed in graphene ribbon after cycles. The variations of peak position, peak shape and intensity are not distinguishable in graphene ribbon after cycles. It indicates that graphene ribbon has excellent structural stability.

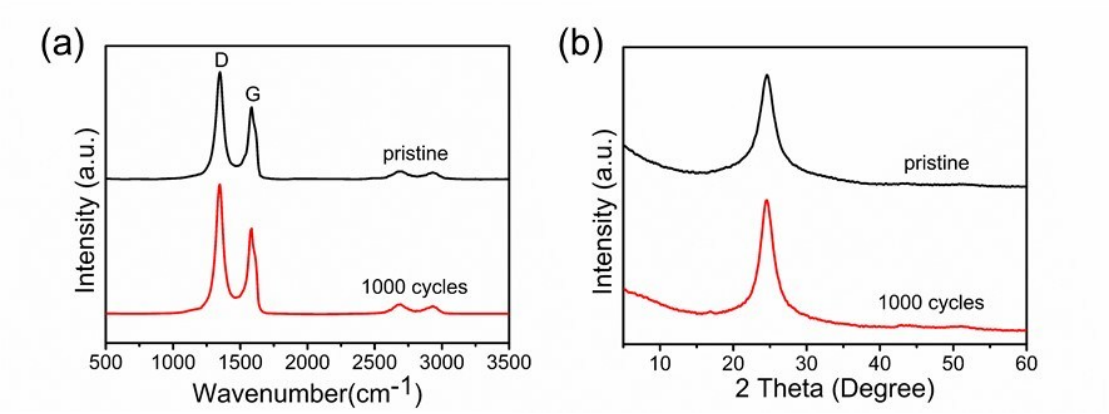

Fig S8 (a) Raman spectra and (b) XRD patterns of graphene aerogel before cycling and after 1000 cycles. No obvious variations in the G and D peak positions were observed in graphene aerogel after cycles. The I_D/I_G ratio increases slightly from 1.49 to 1.51 after cycles. The variations of peak position and peak shape are not distinguishable in graphene aerogel after cycles. Peak intensity increases slightly from 2683 to 3103 after cycles. It indicates that graphene aerogel has favourable structural stability.

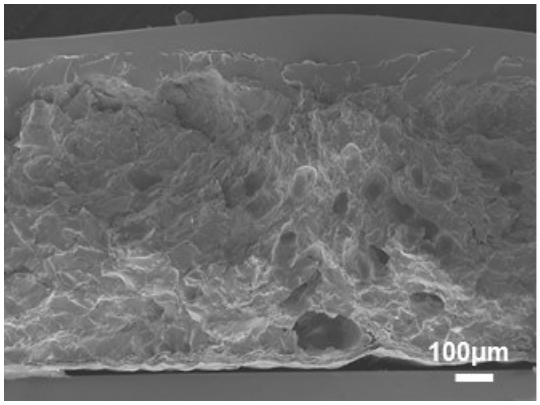

Fig S9 The cross image of tactile sensor with PDMS packaging. The PDMS packaging of tactile sensors is conducive to protect graphene aerogel structure and prevent it damage.

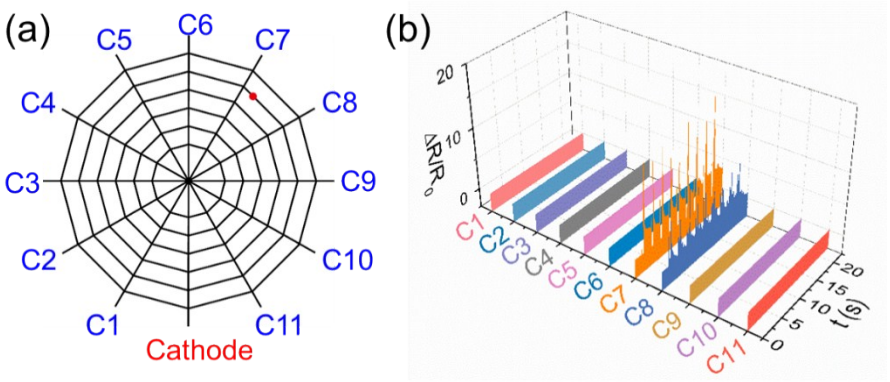

Fig. S10 The real-time monitoring of relative resistance changes ($\Delta R/R_0$) with stimuli by 11 channels (C1-C11). (a) Force points and (b) relative resistance changes ($\Delta R/R_0$) of 11 channels. The results indicate that the resistance change of channel near the force point is remarkable, and the further the distance is, the less the resistance changes.

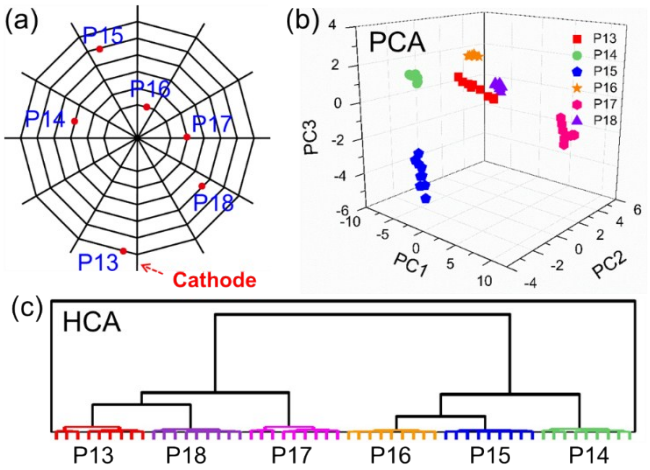

Fig. S11 Electronic discriminant analysis of random positions based on the graphene tactile sensor. (a) Force points, (b) 3D representation of PCA and (c) HCA of P13-P18.

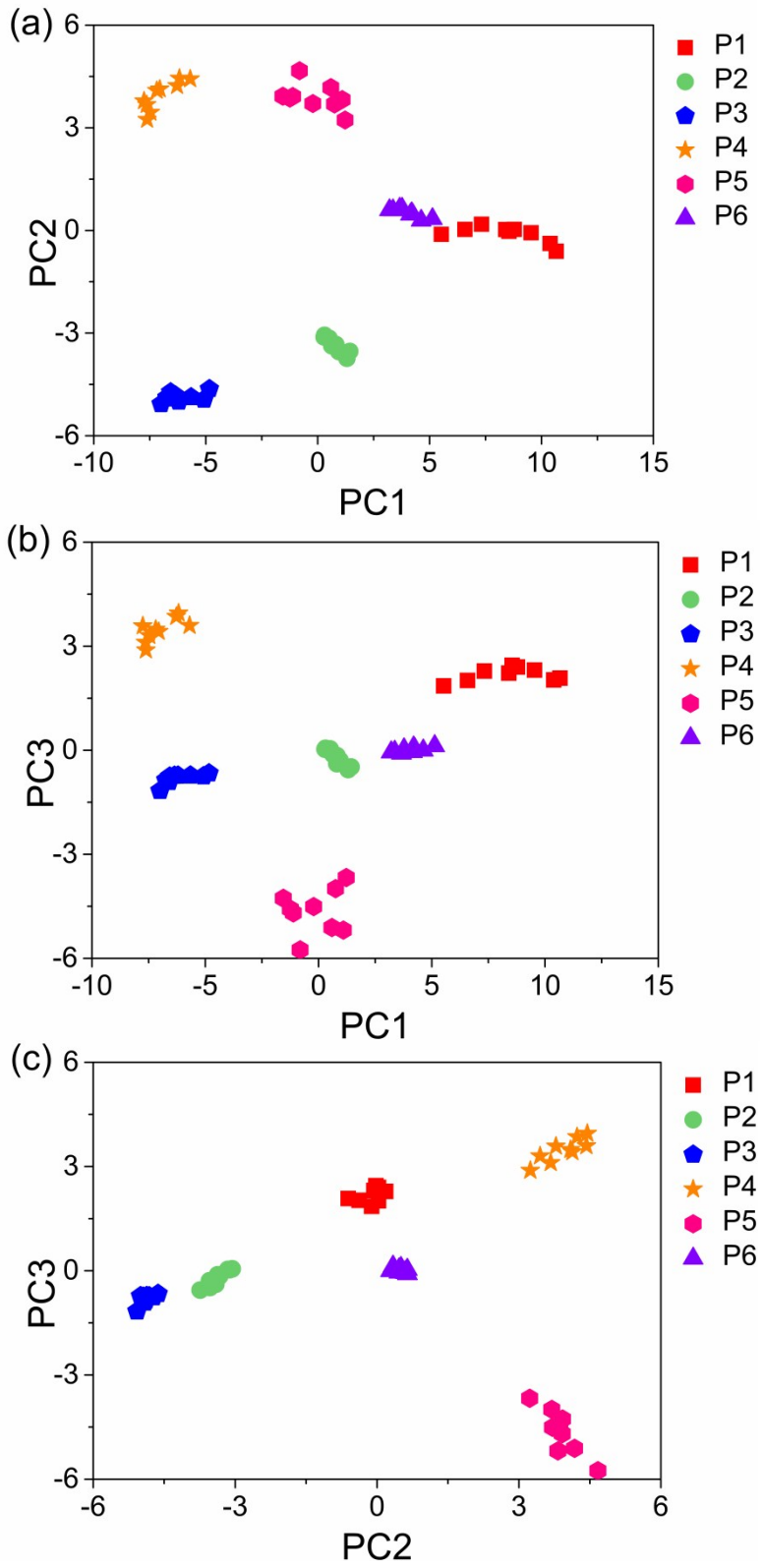

Fig. S12 PCA score plots of the first three principal components of statistical significance for the six points of different orientations at the same distance (P1-P6). (a), (b), (c) represent the PCA result at different projection respectively.

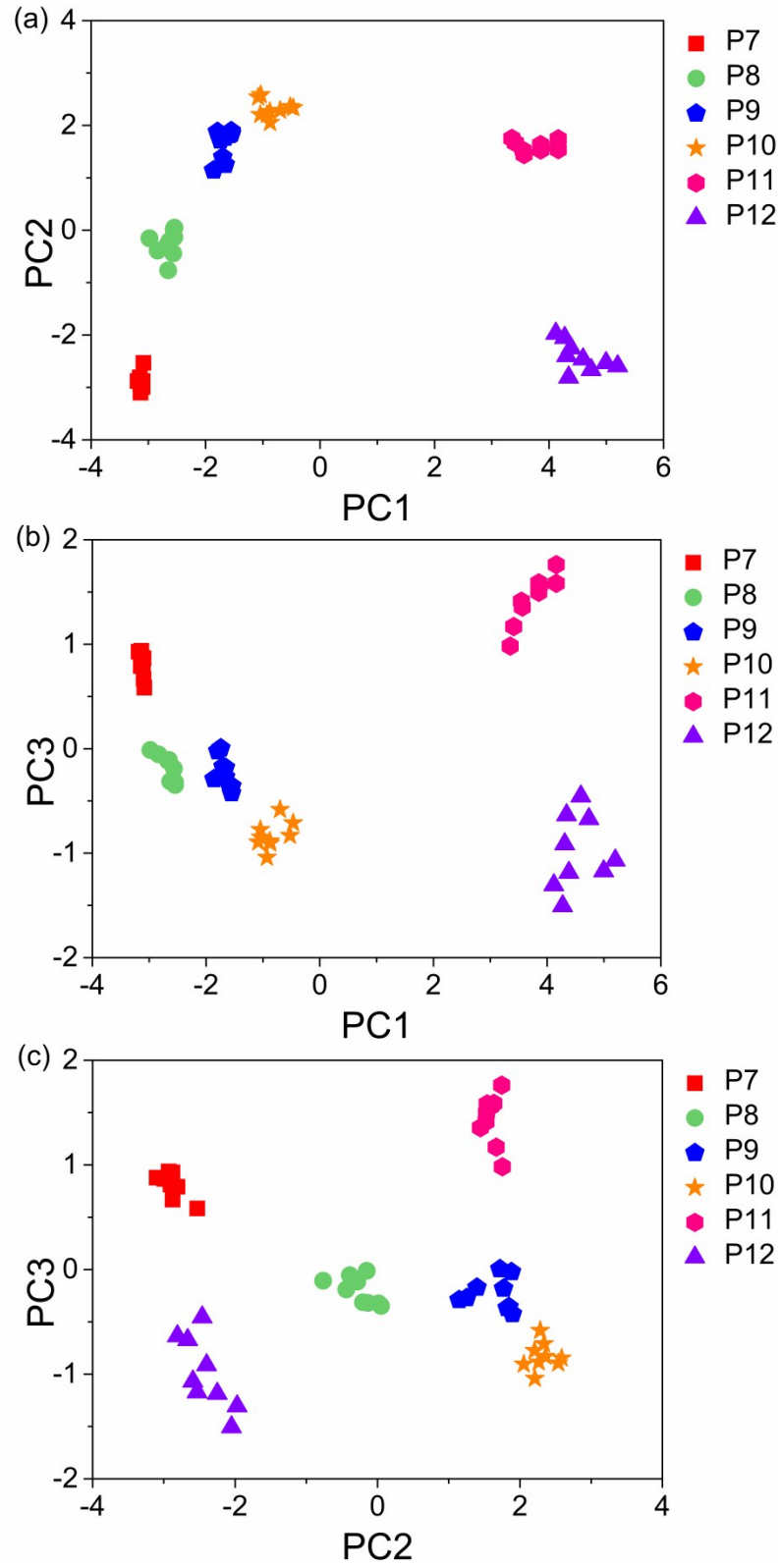

Fig. S13 PCA score plots of the first three principal components of statistical significance for the six points of different distances on the same orientation (P7-P12). (a), (b), (c) represent the PCA result at different projection respectively.

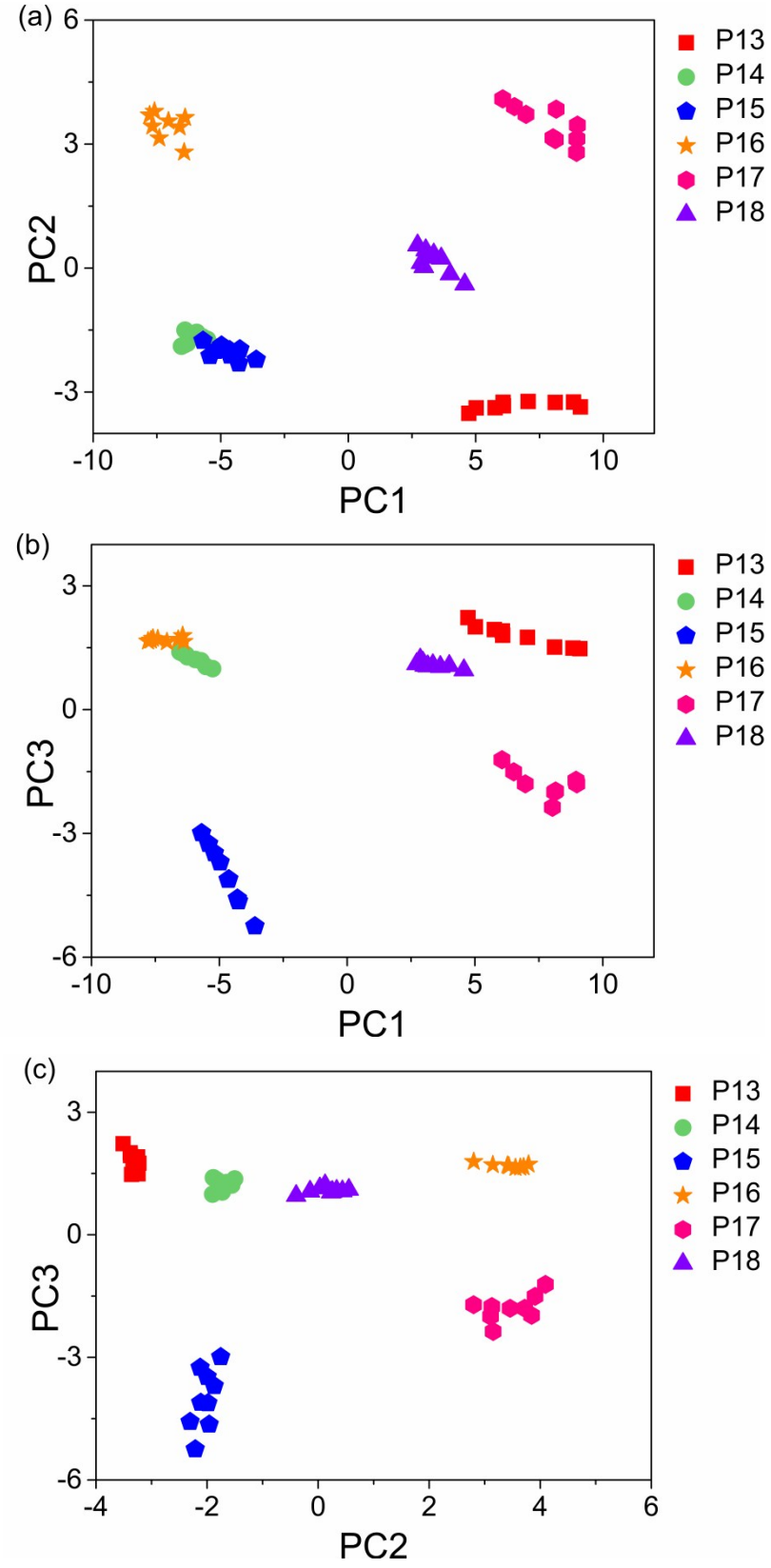

Fig. S14 PCA score plots of the first three principal components of statistical significance for the six points of random distribution (P13-P18). (a), (b), (c) represent the PCA result at different projection respectively.

Table S1 Linear discriminant analysis (LDA) of P1-P12

Classification Matrix on P1-P12													
	P1	P2	P3	P4	P5	P6	P7	P8	P9	P10	P11	P12	Correct
P1	9	0	0	0	0	0	0	0	0	0	0	0	100%
P2	0	9	0	0	0	0	0	0	0	0	0	0	100%
P3	0	0	9	0	0	0	0	0	0	0	0	0	100%
P4	0	0	0	9	0	0	0	0	0	0	0	0	100%
P5	0	0	0	0	9	0	0	0	0	0	0	0	100%
P6	0	0	0	0	0	9	0	0	0	0	0	0	100%
P7	0	0	0	0	0	0	9	0	0	0	0	0	100%
P8	0	0	0	0	0	0	0	9	0	0	0	0	100%
P9	0	0	0	0	0	0	0	0	9	0	0	0	100%
P10	0	0	0	0	0	0	0	0	0	9	0	0	100%
P11	0	0	0	0	0	0	0	0	0	0	9	0	100%
P12	0	0	0	0	0	0	0	0	0	0	0	9	100%
Total	9	9	9	9	9	9	9	9	9	9	9	9	100%
N = 108					N Correct = 108					Proportion Correct = 1.000			

Table S2 Linear discriminant analysis (LDA) of P13-P18

Classification Matrix on P13-P18							
	P13	P14	P15	P16	P17	P18	Correct
P13	9	0	0	0	0	0	100%
P14	0	9	0	0	0	0	100%
P15	0	0	9	0	0	0	100%
P16	0	0	0	9	0	0	100%
P17	0	0	0	0	9	0	100%
P18	0	0	0	0	0	9	100%
Total	9	9	9	9	9	9	100%
N = 54			N Correct = 54			Proportion Correct = 1.000	

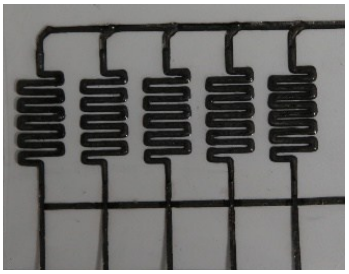

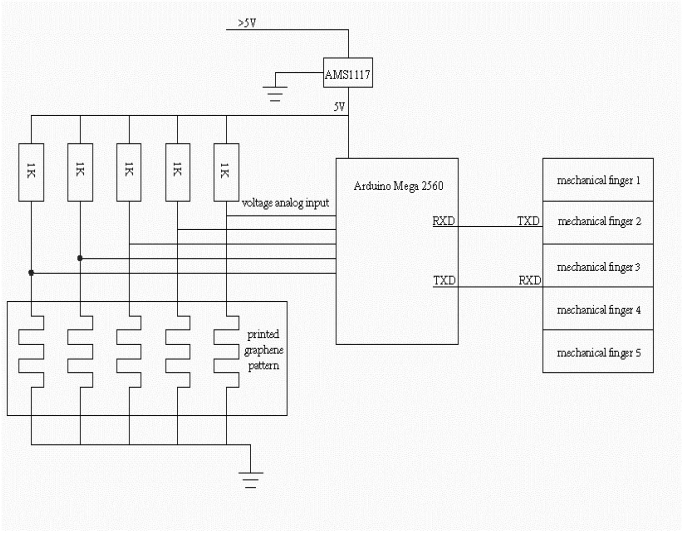

Fig. S15 Control circuit of the mechanical palm.

References

1 B. An, Y. Ma, W. Li, M. Su, F. Li, Y. Song, *Chem. Commun.* 2016, **52**, 10948-10951.
2 W. Li, F. Li, H. Li, M. Su, M. Gao, Y. Li, D. Su, X. Zhang, Y. Song, *ACS Appl. Mater. Interfaces* 2016, **8**, 12369-12376.
3 M. Su, F. Li, S. Chen, Z. Huang, M. Qin, W. Li, X. Zhang, Y. Song, *Adv. Mater*. 2016, **28**, 1369-1374.
4 J. Li, S. Zhao, X. Zeng, W. Huang, Z. Gong, G. Zhang, R. Sun, C.-P. Wong, *ACS Appl. Mater. Interfaces* 2016, **8**, 18954.